

# Hierarchical supercapacitor electrodes based on metallized glass fiber for ultrahigh areal capacitance



Yang Wang<sup>a,b</sup>, Songyang Su<sup>c</sup>, Lejuan Cai<sup>a</sup>, Bocheng Qiu<sup>a</sup>, Cheng Yang<sup>c</sup>, Xiaoming Tao<sup>b,\*</sup>,  
Yang Chai<sup>a,\*</sup>

<sup>a</sup> Department of Applied Physics, The Hong Kong Polytechnic University, Hung Hom, Kowloon, Hong Kong, China

<sup>b</sup> Institute of Textiles and Clothing, The Hong Kong Polytechnic University, Hung Hom, Kowloon, Hong Kong, China

<sup>c</sup> Division of Energy and Environment, Graduate School at Shenzhen, Tsinghua University, Shenzhen 518055, China

## ARTICLE INFO

### Keywords:

Supercapacitor  
Hierarchical electrode  
Metallized glass fiber  
Areal capacitance  
Volumetric capacitance

## ABSTRACT

The limited charge storage of supercapacitors at the surface region results in its high power density but low energy density. It still remains a great challenge to realize supercapacitor electrodes with both bulk-like charge storage (high energy density) and surface-like fast electron/ion kinetics (high power density). Here we demonstrate scalable and hierarchical electrodes by metallizing 3D glass fiber (GF) frameworks and loading with 2D mixed-valence metal oxides. The resulting GF-Ni-Au@NiO<sub>x</sub> cathode and GF-Ni-Au@FeO<sub>x</sub> anode allow fast electron transportation through the conductive networks and unimpeded ion transport through the micrometer channels over long distance, provide large specific surface area with the hierarchical nanostructures, and exhibit ultrahigh areal capacitances (3.57 F cm<sup>-2</sup> for cathode and 3.34 F cm<sup>-2</sup> for anode at the current density of 3 mA cm<sup>-2</sup>). The asymmetric supercapacitor is assembled by employing industrial printed circuit board packaging techniques, showing high areal (1.67 F cm<sup>-2</sup>) and volumetric (13.92 F cm<sup>-3</sup>) capacitances. Remarkably, the device exhibits a maximum energy density of 6.19 mWh cm<sup>-3</sup> and a maximum power density of 334.15 mW cm<sup>-3</sup> based on the total packaged volume of the device. Furthermore, the device shows superior stability during a 400-h continuous test. This hierarchical electrode shows great potential for maintaining high capacity and fast kinetics simultaneously, and can be further extended to other electrochemical energy storage or conversion devices.

## 1. Introduction

The development of transportation and grid storage strongly demands technological breakthrough in energy storage devices with high power density and high energy density simultaneously. One route towards this goal is to realize high energy-density supercapacitors, which possess shorter charging/discharging time and longer cycling life than Li-ion batteries [1–5]. High mass loading of active materials promises a route to increase the energy density and the capacity of a supercapacitor, e.g., the use of thick electrodes to increase the mass loading; and the power density of a supercapacitor is mainly affected by the electrical conductivities for both electrons and ions. While, it is still a fundamental challenge to construct electrodes with efficient ion/electron transport for the thick electrodes with high mass loading of active materials, which usually limits ion transport and increases resistance to electron transport, thus rendering the rapid degradation of capacity retention and the decrease of rate capability [6].

The use of three-dimensional (3D) conductive frameworks as supercapacitor electrode can facilitate the efficient ion/electron transport because of their macroporous structure. Nickel foam, stainless-steel mesh and carbon cloth have been extensively explored since they are highly conductive, commercially available and electrochemically stable [7–9]. But they show a relatively low specific surface area (SSA, less than 0.5 m<sup>2</sup> g<sup>-1</sup>), which limits the volumetric energy density of supercapacitor. Some 3D frameworks made with nanomaterials, e.g., graphene foam and carbon nanotube film, possess a very large SSA value (usually more than 100 m<sup>2</sup> g<sup>-1</sup>) [10,11]. However, their micro-scale pores and channels slow down the kinetics of ion transport. More recently, researchers directly synthesize metal networks [12] or metallize non-conductive 3D frameworks, such as, cellulose paper [5], cotton fabric [13], polystyrene nanofiber [14], textile [15] and carbon fiber [16], to realize high conductivity of supercapacitor electrodes.

The design and construction of hierarchical electrodes enable unimpeded ion transportation and large capacity of a supercapacitor at the same

\* Corresponding authors.

E-mail addresses: [xiao-ming.tao@polyu.edu.hk](mailto:xiao-ming.tao@polyu.edu.hk) (X. Tao), [ychai@polyu.edu.hk](mailto:ychai@polyu.edu.hk) (Y. Chai).

time, where large pores serve as effective ion transportation channels, and micropores provide large SSA. Researchers have loaded various nanostructures onto 3D conductive frameworks, including the double-layer capacitance materials (such as, graphene [17], carbon nanotube [18], activated carbon [19] and other 3D carbon material) and pseudocapacitive ones (e.g., metal oxides [1,20], transition metal dichalcogenides [21], transition metal carbides [22], etc). Among them, two-dimensional (2D) metal oxides exhibit high theoretical capacitance due to their large SSA and abundant electrochemical active sites and transport channels [23,24]. However, it is still a great challenge to make full use of these advantages, especially for the high mass loading over  $2 \text{ mg cm}^{-2}$  [24]. In addition, it is also important to match the capacity of cathode and anode to boost the output power and energy of the supercapacitor [25].

In this work, we adopt commercially available, large-scale and free-standing glass fiber (GF) as the 3D framework, which shows a large SSA ( $2.73 \text{ m}^2 \text{ g}^{-1}$ ). The GF film was metallized by nickel and gold (GF-Ni-Au) through an electroless plating process (Fig. 1a). 2D mixed-valence metal oxides as active materials were assembled onto the 3D GF-Ni-Au frameworks to obtain the GF-Ni-Au@NiO<sub>x</sub> cathode and GF-Ni-Au@FeO<sub>x</sub> anode. The resulting supercapacitor electrodes, with high conductivity, large SSA and hierarchical structure, exhibit high areal capacitances of  $3.57 \text{ F cm}^{-2}$  (GF-Ni-Au@NiO<sub>x</sub>) and  $3.34 \text{ F cm}^{-2}$  (GF-Ni-Au@FeO<sub>x</sub>) at  $3 \text{ mA cm}^{-2}$ . The assembled asymmetric supercapacitor (Fig. S1) exhibits superior areal ( $1.67 \text{ F cm}^{-2}$ ) and volumetric ( $13.92 \text{ F cm}^{-3}$ ) capacitances. This metallized GF film shows the advantages of large scale, high conductivity, high SSA and proper pore distribution, and provides a 3D conductive framework for loading various active materials.

## 2. Experimental

### 2.1. Metallization of the GF film

The metallization process of GF is shown in Fig. 1a(i) and a(ii).

The GF film was purchased from GE Healthcare Life Sciences (Whatman, GF/A), with a thickness of  $260 \mu\text{m}$  and a diameter of  $90 \text{ mm}$ . Firstly, the GF film was cut into small ones with a diameter of  $12 \text{ mm}$ . A small piece was immersed into acetone and ethanol in sequence to clean the surface. Then, it was soaked in  $0.25\%$  HF aqueous solution for  $60 \text{ s}$  to increase the roughness of the fiber surface. A sensitization/activation treatment was carried out to the film in a dark green colloid-palladium solution, which was prepared by dissolving  $0.25 \text{ g PdCl}_2$ ,  $3 \text{ g SnCl}_2$ ,  $10 \text{ mL HCl}$  aqueous solution ( $37\%$ ),  $250 \text{ g NaCl}$ ,  $0.5 \text{ g Na}_2\text{SnO}_3$  and  $50 \text{ g urea}$  into  $1 \text{ L}$  deionized (DI) water. Followed by sensitization and activation treatment for  $5 \text{ min}$ , the GF film was placed into an oven at  $60^\circ\text{C}$  for  $2 \text{ h}$  to remove the water solvent and induce a strong adhesion between the colloid-palladium and the surface of GF. It was subsequently transferred into  $50 \text{ g L}^{-1}$  NaOH aqueous solution for the demicellization process and exposing the active palladium to electroless Ni plating solution.

The electroless Ni plating solution was prepared by adding  $50 \text{ g NiSO}_4 \cdot 6\text{H}_2\text{O}$ ,  $30 \text{ g NaH}_2\text{PO}_2 \cdot \text{H}_2\text{O}$ ,  $18 \text{ g citric acid}$  and  $25 \text{ g CH}_3\text{COONa}$  into  $1 \text{ L}$  Deionized (DI) water. After sufficient dissolving, the pH of the solution was adjusted to  $5.5$  by  $\text{NH}_3 \cdot \text{H}_2\text{O}$ . The solution was then heated to  $66^\circ\text{C}$ . A few pieces of the activated GF films were placed into the solution. The electroless plating duration was kept for  $10 \text{ min}$ . Then the film (designated as GF-Ni film) was washed by DI water and dried in the vacuum oven. The sheet resistance of the GF-Ni film was  $2.6 \Omega \square^{-1}$ .

The electroless plating Au solution was prepared by mixing  $5 \text{ mmol Na}_3\text{Au}(\text{SO}_3)_2$ ,  $0.3 \text{ mol Na}_2\text{SO}_3$ ,  $0.2 \text{ mol Na}_2\text{S}_2\text{O}_3$  and  $0.2 \text{ mol Na}_2\text{HPO}_3$  into  $1 \text{ L}$  DI water, and then the pH of the solution was adjusted to  $6.5$  by sulfuric acid solution. The solution was heated to  $65^\circ\text{C}$ . The GF-Ni films were placed into the solution and the plating duration was  $10 \text{ min}$ . After the Au plating, the obtained products (designated as GF-Ni-Au films) were washed and dried. They showed a sheet resistance of  $1.4 \Omega \square^{-1}$ .

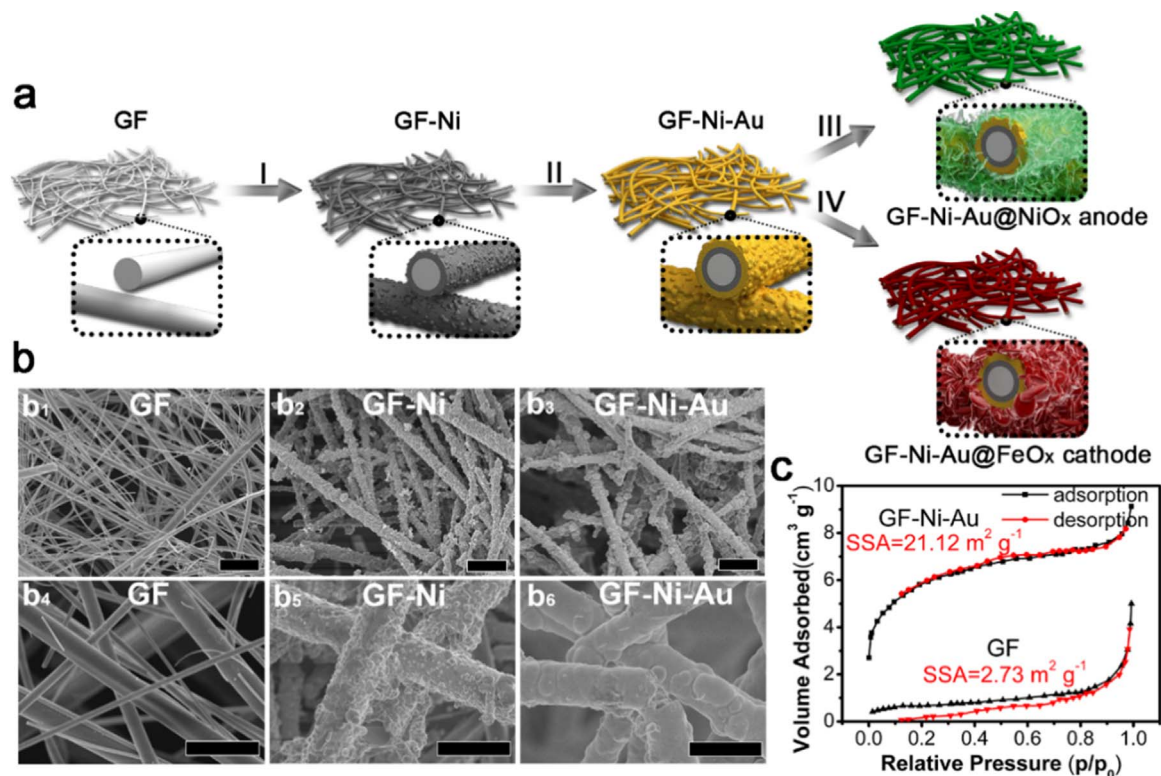


**Fig. 1.** (a) Schematic fabrication process of the cathode and anode: i) Electroless plating Ni onto glass fiber (GF) film; ii) Electroless plating Au onto GF-Ni film; iii) Assembly 2D NiO<sub>x</sub> onto the GF-Ni-Au film; iv) Assembly 2D FeO<sub>x</sub> onto the GF-Ni-Au film. (b) SEM images of the fiber films: b<sub>1–3</sub>) SEM images of GF, GF-Ni and GF-Ni-Au, the scale bar is  $10 \mu\text{m}$ ; b<sub>4–6</sub>) Their enlarged SEM images, respectively, the scale bar is  $5 \mu\text{m}$ . (c) Adsorption isotherm curves of the GF and GF-Ni-Au films. The SSAs are calculated as  $2.73$  (GF) and  $21.12 \text{ m}^2 \text{ g}^{-1}$  (GF-Ni-Au), respectively.

## 2.2. Synthesis of GF-Ni-Au@NiO<sub>x</sub> cathode and GF-Ni-Au@FeO<sub>x</sub> anode

The growth of NiO<sub>x</sub> nanosheets onto the GF-Ni-Au film was conducted by a solution-phase assembly method (Fig. 1a (iii)). 4.5 mmol Ni(NO<sub>3</sub>)<sub>2</sub>·H<sub>2</sub>O and 15 mmol urea were added into 100 mL DI water, to obtain the reaction solution after stirring. Then a few pieces of as-made GF-Ni-Au films were placed into the solution, which was immediately loaded into a vacuum container for 30 min to remove the air bubbles inside the films. Afterwards, the sample was heated to 85 °C and kept for 12 h. The obtained products were collected and washed by DI water for a few times and then dried. Finally, they were placed into an oven and annealed at 300 °C in air for 2 h. The areal mass loading of NiO<sub>x</sub> on GF-Ni-Au was 3.8 mg cm<sup>-2</sup>. The products were designated as GF-Ni-Au@NiO<sub>x</sub> for the cathode.

The fabrication of the anode was similar to that of the cathode (Fig. 1a (iv)). Specially, 4.5 mmol Fe(NH<sub>4</sub>)<sub>2</sub>(SO<sub>4</sub>)<sub>2</sub> and 15 mmol urea were dissolved into 200 mL DI water, and a few as-prepared GF-Ni-Au films were placed into the solution. After a 30-min vacuuming process to remove the air bubbles inside the films, the solution was heated to 36 °C and kept for 12 h. The products were washed and dried, and then annealed at 400 °C in air for 2 h. The areal mass loading of FeO<sub>x</sub> active material on GF-Ni-Au was 4.4 mg cm<sup>-2</sup>. The products were named as GF-Ni-Au@FeO<sub>x</sub> for the anode.

## 2.3. Fabrication of the sandwich-structured supercapacitor

The components of sandwich-structured supercapacitor consist of GF-Ni-Au@FeO<sub>x</sub> anode, GF-Ni-Au@NiO<sub>x</sub> cathode, cellulose fiber separator (thickness of 30 μm), 2 M KOH aqueous electrolyte, one piece of insulating rigid cofferdam (thickness of 700 μm) and two pieces of conductive substrate based on FR4 (epoxy glass fiber) board (thickness of 200 μm). Fig. S1 shows the preparation process of the supercapacitor. First, one piece of FR4 board (epoxy glass fiber board) was successively processed by hole drilling, electroless plating Cu and electroplating Au, where the top and the bottom sides were interconnected by metalized through-holes. This preparation procedure was fully compatible with the printed circuit board (PCB) processing technology. One piece of bare FR4 was then sculptured by high power laser (EP-15-DW, Han's Laser, China) to get a hollow rigid insulating cofferdam. The upside and downside of the cofferdam were then coated with a thin layer of polyurethane-based hot-melt glue (Henkel, Loctite 3542). Afterwards, the anode and cathode were placed onto the conductive substrates, respectively. Those above components, combined with the separator soaked with electrolyte, were mounted together through a delicate lamination system (CUYI, China). The total thickness of the device can be controlled as 1.2 mm.

## 2.4. Materials and device characterizations

The morphology of the above materials was investigated by scanning electron microscopy (SEM, SUPRA 55, ZEISS, Germany) and high-resolution transmission electron microscopy (HR-TEM, JEM 2100F, JEOL, Japan). The elemental analysis was characterized by X-ray photoelectron spectroscopy (XPS, PHI 5000 Versaprobe II, Ulvac-Phi, Japan) and X-ray diffraction (XRD, D8 Advance, Bruker, Germany), separately. The hydrophilicity of the electrodes was conducted on the force tensiometer (K11, Kruss, Germany). The SSA was calculated based on Brunauer–Emmett–Teller (BET) method, obtained at 77 K through an automated adsorption apparatus (ASAP 2020, Micromeritics, America).

The electrochemical performance of the samples, including cyclic voltammetry (CV), galvanostatic charging/discharging (GCD) and electrochemical impedance spectroscopy (EIS), was measured by an electrochemical workstation (VMP3, Bio-Logic, France). The mass/areal/volumetric specific capacitance ( $C_m/C_a/C_v$ ), volumetric specific

energy density ( $E_v$ ) and volumetric specific power density ( $P_v$ ) of the electrodes or supercapacitor were calculated from the CV or GCD curves according to the Eqs. (1)–(4),

$$C_{m(a,v)} = \frac{\int i(U)dU}{m(a, V)v\Delta U} \quad (1)$$

$$C_{m(a,v)} = \frac{i\Delta t}{m(a, V)\Delta U} \quad (2)$$

$$E_{m(v)} = \frac{C_{m(v)}(\Delta U)^2}{2 \times 3600} \quad (3)$$

$$P_{m(v)} = \frac{E_{m(v)}}{\Delta t} \quad (4)$$

where  $i$  is the applied current,  $v$  is the scan rate,  $\Delta t$  is the discharge time,  $\Delta U$  is the operating voltage window, and  $m/a/V$  is the mass/area/volume of the active material, electrode or device.

## 3. Results and discussion

### 3.1. Morphology and structure characterizations

#### 3.1.1. GF, GF-Ni and GF-Ni-Au films

The use of thick electrodes can significantly increase the mass loading close to the requirements of commercial energy storage devices, but severely limit the ion and charge transport, which gives rise to rapid degradation of capacity retention. The macroporous characteristics of commercial GF allow high ion shuttling speed. To enable efficient charge delivery over long distance, we metallized the GF film by Ni and Au, which still maintains their macroporous characteristics, and greatly decreases the charge transfer resistance. Furthermore, the Au coating can also prevent Ni layer from reacting with the electrolyte during the electrochemical cycling, especially in alkaline solutions [26]. We adopt metallized GF with porous structure and large surface area as the free-standing substrate for supercapacitor electrode. Fig. S2 shows the photos of GF, GF-Ni and GF-Ni-Au films, respectively. After the metallization process with Ni and Au, the color of GF changes from white (GF) to dark grey (GF-Ni) and to gold yellow (GF-Ni-Au).

Fig. 1b<sub>1</sub> shows the SEM image of the pristine GF film. The fibers exhibit smooth surface with the diameter in the range of 0.5–2.0 μm, and randomly distribute to form a 3D network. The SSA of GF film, extracted from the adsorption isotherm curve (Fig. 1c), is 2.73 m<sup>2</sup> g<sup>-1</sup>. There are two kinds of pores in the GF film. The large ones at the micrometer level can be obviously observed in the SEM image (Fig. 1b<sub>1</sub>). The size of micro- and mesopores is in the range of 1–100 nm with an average pore size of 10.08 nm, as shown in the Barrett–Joyner–Halenda (BJH) pore size distribution plot (Fig. S3). After the subsequent electroless plating process, the thickness of the GF film increases to over 1 mm with a loose structure. From the SEM images (Figs. 1b<sub>2</sub> and 1b<sub>3</sub>), we can observe that the fibers are densely coated by Ni and Au layer with remarkable roughness, and the fiber diameter increases to approximately 1.5–3.0 μm. Enlarged SEM images of the films (Fig. 1b<sub>4</sub>–b<sub>6</sub>) show that the fibers are welded at the junction points after the electroless plating, which can greatly reduce the junction resistance and facilitate the charge transport in the electrode [27]. The structure of the films was also confirmed through XRD characterization (Fig. S4). The original GF film is a typical SiO<sub>2</sub> material (JCPDS no. 82-0512). After the electroless plating, the characteristic peaks for Ni (JCPDS no. 87-0712) and Au (JCPDS no. 04-0784) appear. The SSA (21.12 m<sup>2</sup> g<sup>-1</sup>) of GF-Ni-Au film can be extracted from the adsorption isotherm curve (Fig. 1c). Its rough surface gives rise to an 8-time increase of the SSA value compared with the pristine GF. The large pores of the GF-Ni-Au at the micrometer level are shown in the SEM image (Fig. 1b<sub>3</sub>). The micro- and mesopore

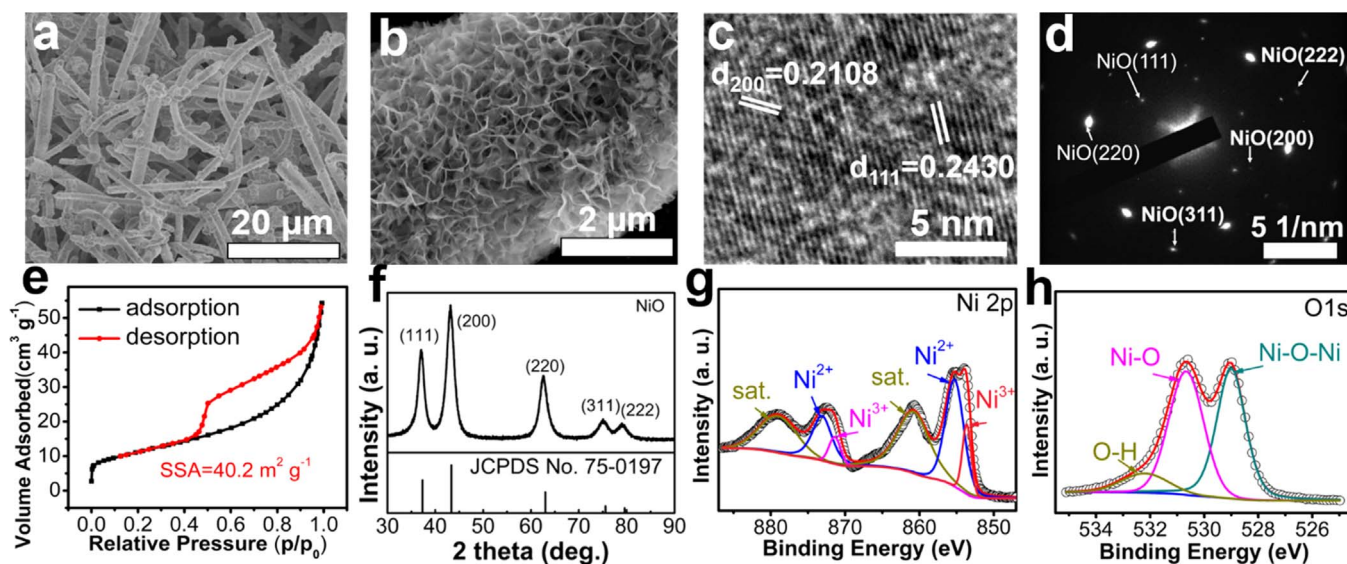


**Fig. 2.** Morphological and structural characterizations of the GF-Ni-Au@NiO<sub>x</sub> cathode. (a) SEM image of the GF-Ni-Au@NiO<sub>x</sub> film; (b) Partial enlarged SEM image of one fiber; (c) HR-TEM image and (d) SEAD pattern of NiO<sub>x</sub>; (e) Adsorption isotherm curve of the GF-Ni-Au@NiO<sub>x</sub> film; (f) XRD spectrum of NiO<sub>x</sub>; (g, h) HR-XPS spectra of Ni 2p and O 1s, respectively.

size distribution is in the range of 1–10 nm with an average pore size of 2.64 nm (Fig. S5).

### 3.1.2. GF-Ni-Au@NiO<sub>x</sub> cathode film

Nickel oxide (NiO<sub>x</sub>) is used as the cathode material due to its high theoretical capacitance, eco-friendliness and low-cost properties [28]. Fig. 2a shows a SEM image of the GF-Ni-Au@NiO<sub>x</sub> film. The fibers form networks with lots of micrometer-scale pores, allowing ions to go across the pores and freely access inner electrode surface over a long distance. Furthermore, most of the fibers are cross-linked to form a 3D network, promoting electrons transport through the electrode. Enlarged crosslinked parts are shown in the SEM images (Fig. S6). Fig. 2b clearly shows that the NiO<sub>x</sub> exhibits a morphology of very thin 2D nanosheets, which intertwine together to form a porous honeycomb structure. Energy-dispersive spectroscopy (EDS) mapping images of one single GF-Ni-Au@NiO<sub>x</sub> fiber show that the Ni, O and Au elements are evenly distributed over the fibers (Fig. S7). Fig. 2c shows the HR-TEM image of the sample. The spaces between two adjacent planes recorded as 0.2108 nm and 0.2430 nm, corresponding to the (200) and

(111) planes of face-centered cubic phase NiO, respectively. Fig. 2d is its selected area electron diffraction (SEAD) image, the ring patterns are consistent with (220), (111), (222), (200) and (311) planes of the NiO.

Due to the hierarchical structure of the film, the SSA of GF-Ni-Au@NiO<sub>x</sub> film greatly increases to 40.2 m<sup>2</sup> g<sup>-1</sup> (Fig. 2e). In addition to the large pores at the micrometer level, the mesopores with size distribution of 1–50 nm and an average pore size of 8.06 nm are observed in the BJH pore size distribution plot (Fig. S8). Contact angle measurement is conducted by sessile drop approach to determine the wettability of the electrode, as shown in video S1. The electrolyte immerses into the GF-Ni-Au@NiO<sub>x</sub> electrode immediately, implying the intimate contact between the super hydrophilic electrode and the electrolyte.

Supplementary material related to this article can be found online at doi:10.1016/j.ensm.2018.11.018.

The XRD pattern of NiO<sub>x</sub> (Fig. 2f) shows the diffraction peaks at 37.04°, 43.12°, 62.70°, 75.07° and 79.04°, well assigned to (111), (200), (220), (311) and (222) crystal planes of face-centered cubic phase NiO (JCPDS no.: 75-0197), respectively, are in good agreement

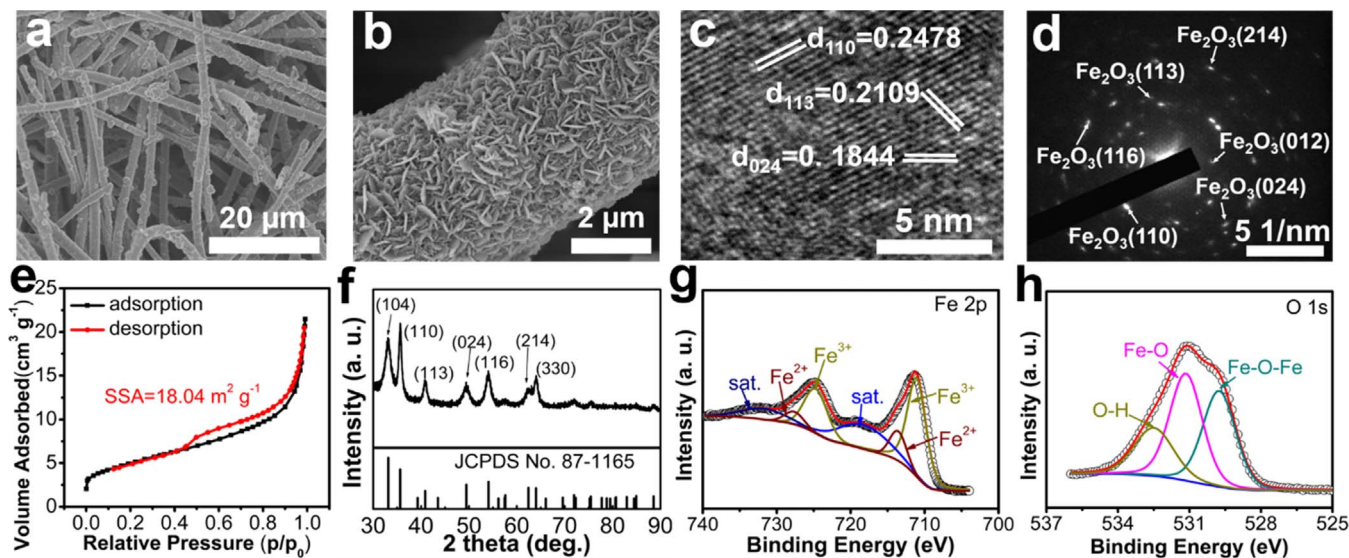


**Fig. 3.** Morphological and structural characterizations of the GF-Ni-Au@FeO<sub>x</sub> anode. (a) SEM image of the GF-Ni-Au@FeO<sub>x</sub> film; (b) Partial enlarged SEM image of one fiber; (c, d) are HR-TEM image and SEAD pattern of FeO<sub>x</sub>; (e) Adsorption isotherm curve of the GF-Ni-Au@FeO<sub>x</sub> film; (f) XRD spectrum of FeO<sub>x</sub>; (g, h) are HR-XPS spectra of Fe 2p and O 1s, respectively.

with the TEM characterization. XPS analysis is used to further confirm the elemental composition and valence state information of the as-obtained sample. The XPS full spectrum (Fig. S9) confirms the existence of Ni and O elements. Fig. 2g and h are the high resolution XPS (HR-XPS) spectra of Ni 2p and O 1s. After the deconvolution, the Ni 2p core level spectrum displays three pairs of typical peaks. The two main peaks of 855.35 eV and 873.10 eV correspond to Ni 2p<sub>3/2</sub> and Ni 2p<sub>1/2</sub>, and the energy separation of 17.75 eV further verifies the existence of Ni<sup>2+</sup>. In addition, the two peaks at binding energies of 879.23 eV and 860.98 eV are shake-up satellite peaks along with the Ni 2p doublets. The presence of two additional deconvoluted peaks at 871.48 eV and 853.60 eV are assigned to the core levels of Ni<sup>3+</sup> cations [29]. The three peaks in Fig. 2h at binding energies of 528.98 eV, 530.73 eV and 532.23 eV are from the Ni–O–Ni, Ni–O and H–O bonds, respectively. From the HR-TEM image in Fig. S10, some appeared amorphous phase areas are speculated to be the subsidiary Ni<sub>2</sub>O<sub>3</sub>, which is in good agreement with the XPS result. The mixed-valence state of NiO<sub>x</sub> can provide multiple electrochemical reaction paths and enhance energy storage capacity [30].

### 3.1.3. GF-Ni-Au@FeO<sub>x</sub> anode film

It is important to match the capacity of anode and cathode to boost the output energy and power of the supercapacitors. Iron oxide exhibits a comparable theoretical capacitance to nickel oxide, and shows low cost, natural abundance and eco-friendliness properties [20,31]. Fig. 3a

shows a SEM image of GF-Ni-Au@FeO<sub>x</sub>. The fibers are well crosslinked and show large pores at the micrometer level. From the partial enlarged SEM image in Fig. 3b, the 2D FeO<sub>x</sub> sheet is much thicker than NiO<sub>x</sub>, leading to a smaller SSA of 18.04 m<sup>2</sup> g<sup>-1</sup> (Fig. 3e) for GF-Ni-Au@FeO<sub>x</sub> compared with the GF-Ni-Au@NiO<sub>x</sub>. The micro- and mesopores show the size distribution of 1–60 nm with an average pore size of 7.27 nm (Fig. S11). From the HR-TEM image (Fig. 3c), we can clearly obtain the planes of (110), (113) and (024), which correspond to the spaces between two adjacent planes of 0.2478 nm, 0.2109 nm and 0.1844 nm, respectively. In addition, we can obtain all the typical planes of α-Fe<sub>2</sub>O<sub>3</sub> from the SEAD pattern (Fig. 3d). Contact angle measurement in video S2 also proves the super hydrophilicity of this anode.

Supplementary material related to this article can be found online at doi:10.1016/j.ensm.2018.11.018.

Fig. 3f is the XRD spectrum of FeO<sub>x</sub>. The main diffraction peaks are perfectly corresponding to the standard sample of α-Fe<sub>2</sub>O<sub>3</sub> (JCPDS no.: 87-1165). The full XPS spectrum of FeO<sub>x</sub> is shown in Fig. S12. High-resolution Fe 2p spectrum (Fig. 3g) shows three pair of typical peaks, belonging to Fe<sup>3+</sup>, Fe<sup>2+</sup> and the shakeup satellite peaks [32]. Combined with the O 1s spectrum (Fig. 3h), these two XPS spectra confirm the mixed valence of the Fe element. Furthermore, the amorphous phase appears in the HR-TEM image of Fig. S13 is speculated to be the subsidiary FeO, which is in good agreement with the XPS results. Similar to NiO<sub>x</sub>, this mixed-valence state feature of FeO<sub>x</sub> can also enhance its energy storage ability.

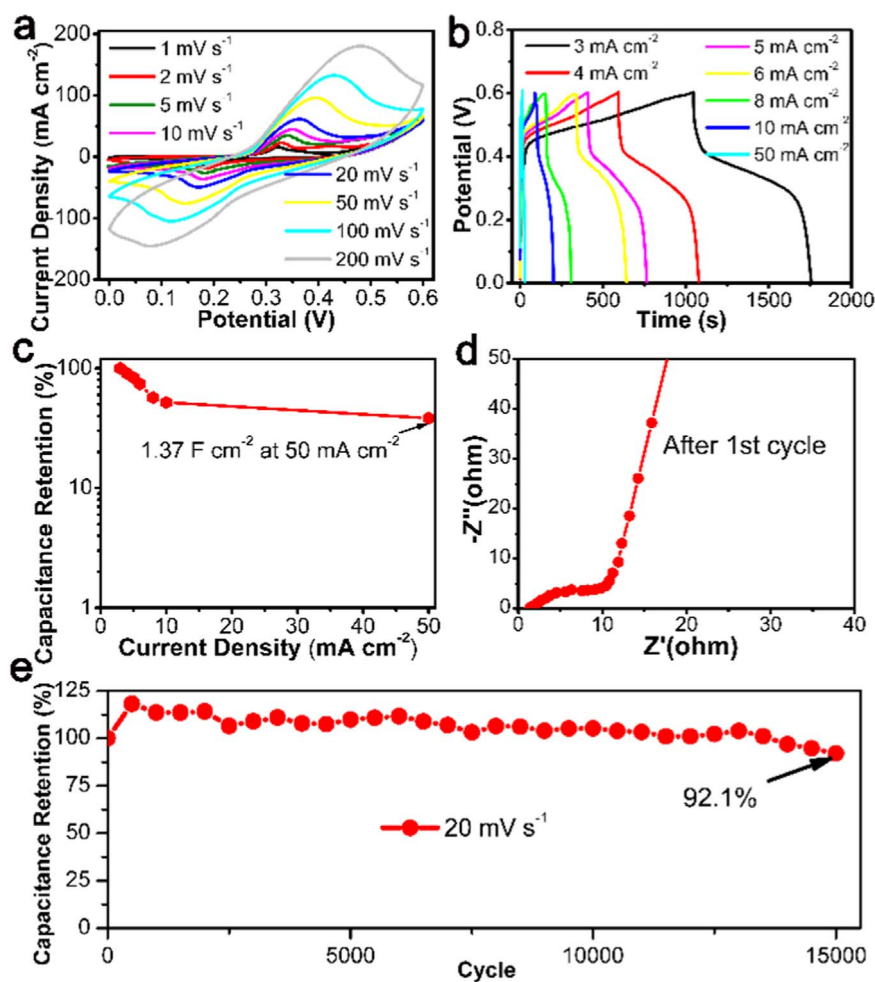


**Fig. 4.** Electrochemical performance of the GF-Ni-Au@NiO<sub>x</sub> cathode. (a) CV curves at the scan rates ranging from 1 mV s<sup>-1</sup> to 200 mV s<sup>-1</sup>; (b) GCD curves at current densities range of 3–50 mA cm<sup>-2</sup>; (c) Capacitance retention versus current density of the cathode calculated by GCD curves; (d) Nyquist curve after the first cycle and (e) Cycling stability test for 15,000 cycles at 20 mV s<sup>-1</sup>.

### 3.2. Electrochemical characterizations

#### 3.2.1. GF-Ni-Au@NiO<sub>x</sub> cathode

The electrochemical test of GF-Ni-Au@NiO<sub>x</sub> was characterized in a three-electrode cell configuration in 2 M KOH electrolyte, where a Pt plate as the counter electrode and a standard Hg/HgO electrode as the reference. The working potential window is determined in the range of 0–0.6 V, where the electrode exhibits a purely capacitive behavior. Fig. 4a shows the cyclic voltammetry (CV) curves of GF-Ni-Au@NiO<sub>x</sub> at scan rates ranging from 1 to 200 mV s<sup>-1</sup>. A number of pairs of redox peaks display symmetrically in each CV curve, indicating the redox behavior. The positions of peaks slightly shift away from the symmetrical center with the increase of scan rate, which is attributed to the change of the internal resistance during the reversible Faradaic reaction [30]. The  $C_a$  value of the cathode is calculated as 3.14 F cm<sup>-2</sup> at the scan rate of 1 mV s<sup>-1</sup>, corresponding to a  $C_m$  value is 826 F g<sup>-1</sup> by normalizing to mass loading. In addition, the CV curve remains in shape that clearly shows the pair of redox peaks even at a high scan rate of 200 mV s<sup>-1</sup>, because of the high-efficient ion and electron transport during the reversible Faradaic reaction.

Galvanostatic charging/discharging (GCD) tests were conducted at current densities in the range of 3–50 mA cm<sup>-2</sup>, as shown in Fig. 4b. The pair of pronounced voltage plateaus in the curves further indicate the redox effect, which is consistent with the redox peaks in the CV results. The redox reaction occurs at the interface of NiO<sub>x</sub> nanosheets and KOH electrolyte, as described in Eq. (5).



This electrochemical reaction mainly involves the valence state change of Ni<sup>2+</sup> cations [28]. When charging to the electrode, the redox reaction occurs at the interface between the electrolyte and NiO<sub>x</sub> along with the change from Ni<sup>2+</sup> to Ni<sup>3+</sup>. During the discharging process, the Ni<sup>3+</sup> returns to Ni<sup>2+</sup>. The  $C_a$  is calculated as 3.57 F cm<sup>-2</sup> at the current density of 3 mA cm<sup>-2</sup>, corresponding to a  $C_m$  of 939 F g<sup>-1</sup>. The  $C_m$  value of GF-Ni-Au@NiO<sub>x</sub> cathode is compared to most of the reported results in spite of high mass loading and high scan rate in our sample. For example, Li et al. coated NiO onto Ni foam substrate with a mass loading of 2.7 mg cm<sup>-2</sup>, exhibiting a  $C_m$  of 392 F g<sup>-1</sup> at the current density of 0.5 mA cm<sup>-2</sup> [33]. The capacitance decreases with the increase of current density (Fig. 4c) because slow redox behavior results in non-equilibrium charge storage status at high current density. Remarkably, the GF-Ni-Au@NiO<sub>x</sub> cathode still remains a  $C_a$  of 1.37 F cm<sup>-2</sup> even at the current density of 50 mA cm<sup>-2</sup>.

The frequency response analysis was conducted in the range of 10 mHz to 100 kHz with an amplitude of 5 mV to investigate the intrinsic impedance of the GF-Ni-Au@NiO<sub>x</sub> cathode. By calculating from the Nyquist plot (Fig. 4d), the equivalent series resistance (ESR) of the electrode is as low as 1.35 Ω, indicating its potential to deliver fast electron response. In addition, measurement of the cycle stability was conducted by repeating the CV test at the scan rate of 20 mV s<sup>-1</sup> (Fig. 4e). After a continuous testing of 15,000 cycles (uninterrupted

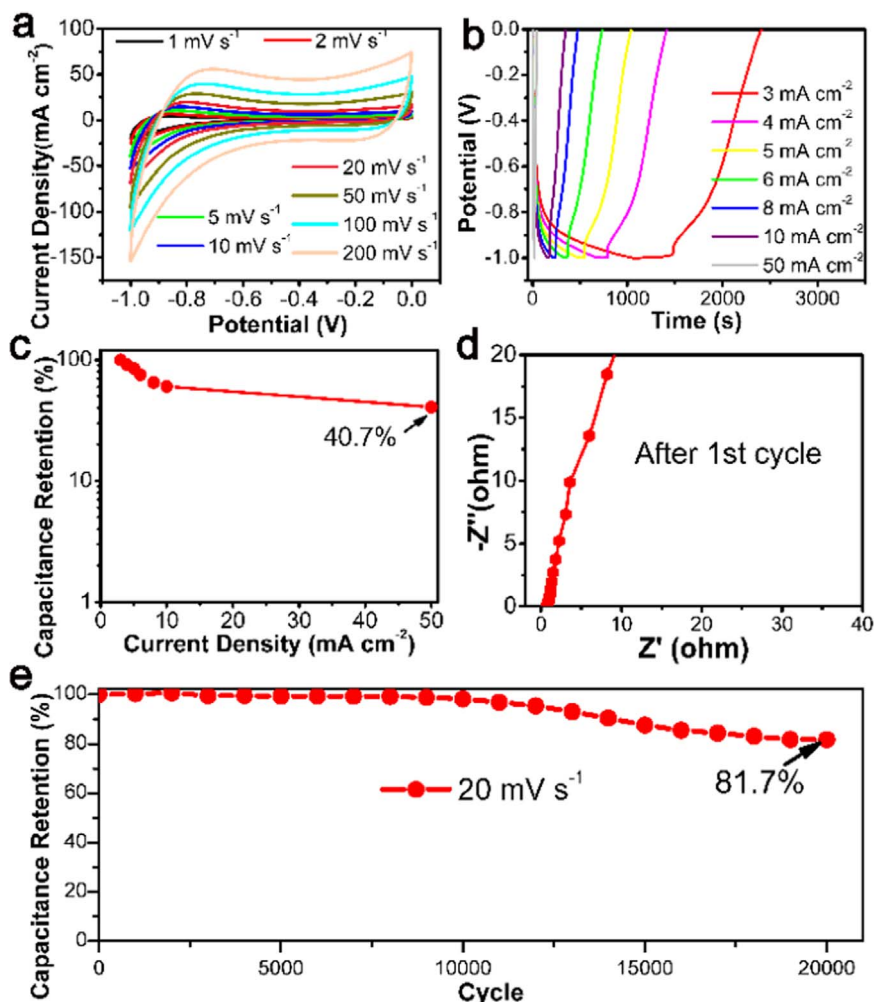


**Fig. 5.** Electrochemical performance of the GF-Ni-Au@FeO<sub>x</sub> anode. (a) CV curves at the scan rates ranging from 1 mV s<sup>-1</sup> to 200 mV s<sup>-1</sup>; (b) GCD curves at current densities range of 3–50 mA cm<sup>-2</sup>; (c) Capacitance retention versus current density of the anode calculated by GCD curves; (d) Nyquist curve after the first cycle and (e) Cycle stability test for 20,000 cycles at 20 mV s<sup>-1</sup>.

working of 250 h), the capacitance retention of the cathode still remains 92.1%.

### 3.2.2. GF-Ni-Au@FeO<sub>x</sub> anode

To fabricate an anode that can match well with the GF-Ni-Au@NiO<sub>x</sub> cathode, we grew FeO<sub>x</sub> nanosheets onto the GF-Ni-Au film using a solution phase synthesis method. The areal mass loading of FeO<sub>x</sub> material in the anode is 4.4 mg cm<sup>-2</sup>. We performed its electrochemical test in a three-electrode cell in 2 M KOH electrolyte, with a working potential window of -1.0 to 0 V. Fig. 5a is the CV result in the range of 1–200 mV s<sup>-1</sup>. The C<sub>a</sub> value is calculated to be 2.48 F cm<sup>-2</sup> at the scan rate of 1 mV s<sup>-1</sup>, corresponding to a C<sub>m</sub> value of 564 F g<sup>-1</sup>. The pseudocapacitive effect at the interface between FeO<sub>x</sub> nanosheets and KOH electrolyte remains elusive at current stage. Some researchers attribute the capacitance to the intercalation and deintercalation of the K<sup>+</sup> cations [34]. Others propose that the OH<sup>-</sup> is involved in the charge-discharge cycling by tuning the valence state of the Fe<sup>3+</sup> cations [35]. The C<sub>a</sub> value calculated from the discharge curves (Fig. 5b) is as high as 3.34 F cm<sup>-2</sup> at the current density of 3 mA cm<sup>-2</sup>. Fig. 5c reveals a similar current-dependent trend for the cathode. A capacitance retention value of 40.7% (corresponding to a C<sub>m</sub> of 1.36 F cm<sup>-2</sup>) is obtained at the current density of 50 mA cm<sup>-2</sup>. These promising electrochemical results manifest that FeO<sub>x</sub> have great potential as the anode material of high performance supercapacitors. Further measurement about electrochemical impedance spectroscopy (EIS, Fig. 5d) of the anode shows the ESR is as low as 0.8 Ω, indicating its fast electrochemical response. Long term cycling of 20,000 cycles at the scan rate of 20 mV s<sup>-1</sup> (Fig. 5e) verifies its excellent stability.

The NiO<sub>x</sub> and FeO<sub>x</sub> samples on pure GF and Ni foil are also prepared by the same solution-phase assembly method for comparison purpose. The electrochemical properties of control samples are tested by CV curves at the scan rate of 50 mV s<sup>-1</sup> (Fig. S14). The capacitances of the samples based on GF@Ni@Au framework are at least 6 times larger than that of the control samples.

### 3.2.3. Asymmetric supercapacitor

For a thick electrode with high mass loading, it is more accurate to evaluate the performance of a supercapacitor by the areal or volumetric

value [36]. From a device perspective, the key issues to improve the electrochemical performance of the supercapacitor include the increase of the mass loading (corresponding to the areal capacitance) and the match of anode and cathode capacity. The overall capacitance of supercapacitor is from the series of two capacitors at the cathode and anode. The mismatch of capacitance results in the decrease of overall capacitance and uneven distribution of the full potential window will be across the two electrodes [25]. According to the previous three electrode measurements, the C<sub>a</sub> values of cathode and anode are 3.57 F cm<sup>-2</sup> and 3.34 F cm<sup>-2</sup> at a current density of 3 mA cm<sup>-2</sup>, respectively, which are very close. We integrate the GF-Ni-Au@NiO<sub>x</sub> cathode and the GF-Ni-Au@FeO<sub>x</sub> anode as a supercapacitor by a printed circuit board (PCB) processing technology.

From the CV curves (Fig. 6a), we can obtain the areal capacitance of 1.57 F cm<sup>-2</sup> at the scan rate of 1 mV s<sup>-1</sup>. A few pairs of peaks in the CV curves are due to the redox reactions at the cathode and anode. The areal capacitance of the supercapacitor can be as large as 1.67 F cm<sup>-2</sup> from the GCD curves (Fig. 6b and Fig. S15) at the current density of 3 mA cm<sup>-2</sup>, slightly higher than the result calculated from the CV curve at the scan rate of 1 mV s<sup>-1</sup>. The specific volumetric capacitance of the supercapacitor, calculated from the GCD curve, is 13.92 F cm<sup>-3</sup> based on all the packaged volume. Fig. 6c shows the capacitance retention of 40.5% when the applied current density of the device is increased to 50 mA cm<sup>-2</sup>. The supercapacitor can maintain a superior specific volumetric capacitance of 5.64 F cm<sup>-3</sup> even at such high scan rate. There is a typical semicircle shown in the high frequency region of the Nyquist plot (Fig. 6d), which is a representation of the interfacial charge transfer resistance. Calculated from the Nyquist plot, the ESR of the device is 4.4 Ω, indicating its excellent electrochemical response at high frequency range. The low resistance also suggests efficient charge transfer at the interface between electrode and electrolyte. The proper pore distribution benefits ion transportation. These characteristics correspond to the small voltage drop at the beginning of the GCD curves [37]. In the low frequency range, the curve exhibits almost a vertical line, indicating an ideal behavior of the supercapacitor. After successive cycling of 400 h (9000 cycles) by CV test and 10,000 cycles by GCD study, the capacitance retention of the supercapacitor can maintain 80.7% (Fig. 6e) and 90.2% (Fig. S16), respectively. In

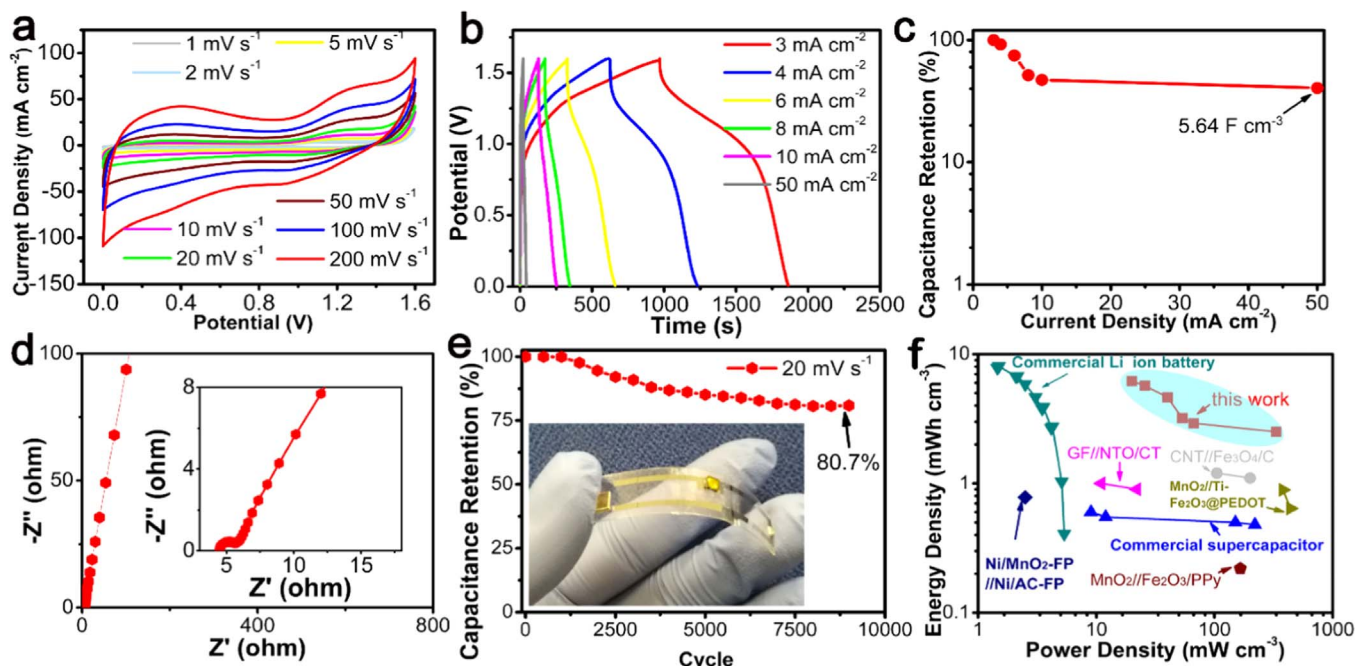


Fig. 6. Electrochemical performance of the full device. (a) CV curves at scan rates of 1–200 mV s<sup>-1</sup>; (b) GCD curves at current densities ranging from 3 to 50 mA cm<sup>-2</sup>; (c) Capacitance retention value versus current density calculated by GCD study; (d) Nyquist curve after one cycle; (e) Cycling stability test of the device at 20 mV s<sup>-1</sup>, inset is our supercapacitor, a LED and a switch are assembled onto a flexible PCB; (f) Ragone plot of our supercapacitor as compared to other recently-reported ones.

addition to the essential features of highly conductive network and moderate porous structure of the GF-Ni-Au current collector, its high mass loading and good electrode matching properties synergistically bring about the outstanding electrochemical results of the supercapacitor.

To evaluate the energy and power properties of the supercapacitor, the related parameters calculated from the GCD curves are presented in the Ragone plot (Fig. 6f). Our device exhibits a maximum  $E_v$  value of  $6.19 \text{ mWh cm}^{-3}$  at the  $P_v$  of  $20.02 \text{ mW cm}^{-3}$ , and maintains an  $E_v$  of  $2.51 \text{ mWh cm}^{-3}$  at the tested maximum  $P_v$  of  $334.15 \text{ mW cm}^{-3}$ . We compare these figures of merit with some of recently reported energy storage devices, including typical Li ion battery (4 V, 500 mA h) [38], CNT//Fe<sub>3</sub>O<sub>4</sub>/C [35], GF//NTO/CT [39], MnO<sub>2</sub>//Ti-Fe<sub>2</sub>O<sub>3</sub>@PEDOT [31], Ni/MnO<sub>2</sub>-FP//Ni/AC-FP [40], MnO<sub>2</sub>//Fe<sub>2</sub>O<sub>3</sub>/PPy [7] and commercial supercapacitor (5.5 V, 100 mF) [35]. Most of them are fabricated based on 3D current collectors. The  $P_v$ - $E_v$  curve (Fig. 6f) of our as-prepared device is positioned on the top right corner of this plot. Its maximum  $E_v$  is compatible to the commercial Li ion battery (4 V, 500 mA h) while delivering a 10-time higher  $P_v$ . Its maximum  $P_v$  can reach the level of commercial supercapacitor (5.5 V, 100 mF) with one order of magnitude larger  $E_v$ . Table S1 documents the comparison of some recently-reported energy storage devices in details, including  $C_a$ ,  $C_v$ , maximum energy density ( $E_{max}$ ) and maximum power density ( $P_{max}$ ). Our device exhibits a comparable  $P_{max}$  and an outperforming  $E_{max}$  among all the devices. Remarkably, the  $C_v$  of our device is outstanding among them even when the total packaging volume is included. Moreover, the  $C_a$ -index is several to dozens of times higher than the others.

By combining with these typical industrial processing technologies (hole drilling, electroless plating and electro plating, and PCB packaging), we obtain supercapacitors with various shapes and different sizes. They have square and circle shapes with side lengths or diameters of 0.2 cm, 0.4 cm, 0.6 cm, 0.8 cm, 1.0 cm, 1.2 cm, 1.4 cm, respectively, as shown in Fig. S17b. Due to the volume-tunability of the device, to match the size of the flexible PCB, we assemble the 0.4 cm ones with an LED and a switch onto a flexible PCB by silver paste, as shown in the inset of Fig. 6e. After charging for a while, both of them can drive the red LEDs, as shown in Figs. S17a and S17c.

#### 4. Conclusions

In summary, we demonstrate a scalable fabrication route by metallizing commercially available GF for the free-standing supercapacitor electrodes. Their hierarchically macroporous and mesoporous structures can not only facilitate the free access of ion transport to the interior and exterior surface of the film and shuttling across the channels, but also provide a large SSA for high mass loading of the active materials. The high conductive and hierarchical feature of the 3D metallized framework enable highly efficient ion and charge transport. In addition, these binder-free, 3D electrodes can effectively release stresses caused by volume expansion/shrinkage during the charge-discharge cycles. All the above merits make them attractive as promising electrodes for supercapacitors. Furthermore, the 3D conductive framework presented here is applicable to a wide range of electrode materials. Combined with the industrial packaging technologies, we efficiently obtain a series of high-reliable and high-performance asymmetric supercapacitors. The above-mentioned features of the devices illustrate great potential close to practical applications.

#### Acknowledgment

This work was supported by Research Grant Council of Hong Kong, Hong Kong (Grant nos. PolyU 152145/15E, 15211016E, and 15200917), the Hong Kong Polytechnic University, Hong Kong (Grant no.: 1-BBA3), National Natural Science Foundation of China, China (Project no.: 51607102), Natural Science Foundation of Guangdong Province, China

(Project no.: 2017A030313279) and Shenzhen Government, China (Project nos. JCYJ20170412171720306 & JCYJ20170412171430026).

#### Appendix A. Supplementary material

Supplementary data associated with this article can be found in the online version at doi:10.1016/j.ensm.2018.11.018.

#### References

- [1] K.A. Owusu, L. Qu, J. Li, Z. Wang, K. Zhao, C. Yang, K.M. Hercule, C. Lin, C. Shi, Q. Wei, L. Zhou, L. Mai, Low-crystalline iron oxide hydroxide nanoparticle anode for high-performance supercapacitors, *Nat. Commun.* 8 (2017) 14264.
- [2] M. Salanne, B. Rotenberg, K. Naoi, K. Kaneko, P.L. Taberna, C.P. Grey, B. Dunn, P. Simon, Efficient storage mechanisms for building better supercapacitors, *Nat. Energy* 1 (2016) 16070.
- [3] N.A. Kyeremateng, T. Brousse, D. Pech, Microsupercapacitors as miniaturized energy-storage components for on-chip electronics, *Nat. Nanotechnol.* 12 (2017) 7–15.
- [4] D. Sheberla, J.C. Bachman, J.S. Elias, C.J. Sun, Y. Shao-Horn, M. Dincă, Conductive MOF electrodes for stable supercapacitors with high areal capacitance, *Nat. Mater.* 16 (2017) 220–224.
- [5] Y. Ko, M. Kwon, W.K. Bae, B. Lee, S.W. Lee, J. Cho, Flexible supercapacitor electrodes based on real metal-like cellulose papers, *Nat. Commun.* 8 (2017) 536.
- [6] H. Sun, L. Mei, J. Liang, Z. Zhao, C. Lee, H. Fei, M. Ding, J. Lau, M. Li, C. Wang, X. Xu, G. Hao, B. Papandrea, I. Shakir, B. Dunn, Y. Huang, X. Duan, Three-dimensional holey-graphene/niobia composite architectures for ultrahigh-rate energy storage, *Science* 356 (2017) 599–604.
- [7] L. Wang, H. Yang, X. Liu, R. Zeng, M. Li, Y. Huang, X. Hu, Constructing hierarchical tectorum-like alpha-Fe<sub>2</sub>O<sub>3</sub>/PPy nanoarrays on carbon cloth for solid-state asymmetric supercapacitors, *Angew. Chem. Int. Ed. Engl.* 56 (2017) 1105–1110.
- [8] N. Choudhary, C. Li, J. Moore, N. Nagaiah, L. Zhai, Y. Jung, J. Thomas, Asymmetric supercapacitor electrodes and devices, *Adv. Mater.* 29 (2017).
- [9] R.R. Salunkhe, B.P. Bastakoti, C.T. Hsu, N. Suzuki, J.H. Kim, S.X. Dou, C.C. Hu, Y. Yamauchi, Direct growth of cobalt hydroxide rods on nickel foam and its application for energy storage, *Chemistry* 20 (2014) 3084–3088.
- [10] Y. Wang, X. Yang, A.G. Pandolfo, J. Ding, D. Li, High-rate and high-volumetric capacitance of compact graphene-polyaniline hydrogel electrodes, *Adv. Energy Mater.* 6 (2016) 1600185.
- [11] M.F. El-Kady, Y. Shao, R.B. Kaner, Graphene for batteries, supercapacitors and beyond, *Nat. Rev. Mater.* 1 (2016) 16033.
- [12] C. Xu, Z. Li, C. Yang, P. Zou, B. Xie, Z. Lin, Z. Zhang, B. Li, F. Kang, C.P. Wong, An ultralong, highly oriented nickel-nanowire-array electrode scaffold for high-performance compressible pseudocapacitors, *Adv. Mater.* 28 (2016) 4105–4110.
- [13] Y. Yang, Q. Huang, L. Niu, D. Wang, C. Yan, Y. She, Z. Zheng, Waterproof, ultrahigh areal-capacitance, wearable supercapacitor fabrics, *Adv. Mater.* 29 (2017).
- [14] K.Y. Park, B. Ramaraj, W.S. Choi, K.R. Yoon, Fabrication and metallization of 3D electrospun nanofibrous architecture with gold and silver coating for applications related to electrochemical supercapacitors, *Mater. Chem. Phys.* 142 (2013) 600–607.
- [15] W.C. Li, C.L. Mak, C.W. Kan, C.Y. Hui, Enhancing the capacitive performance of a textile-based CNT supercapacitor, *RSC Adv.* 4 (2014) 64890–64900.
- [16] L. Gao, J.U. Surjadi, K. Cao, H. Zhang, P. Li, S. Xu, C. Jiang, J. Song, D. Sun, Y. Lu, Flexible fiber-shaped supercapacitor based on nickel-cobalt double hydroxide and pen ink electrodes on metallized carbon fiber, *ACS Appl. Mater. Interfaces* 9 (2017) 5409–5418.
- [17] R. Raccichini, A. Varzi, S. Passerini, B. Scrosati, The role of graphene for electrochemical energy storage, *Nat. Mater.* 14 (2015) 271–279.
- [18] R. Kumar, R.K. Singh, P.K. Dubey, D.P. Singh, R.M. Yadav, Self-assembled hierarchical formation of conjugated 3D cobalt oxide nanobead-CNT-graphene nanostructure using microwaves for high-performance supercapacitor electrode, *ACS Appl. Mater. Interfaces* 7 (2015) 15042–15051.
- [19] L. Qie, W. Chen, H. Xu, X. Xiong, Y. Jiang, F. Zou, X. Hu, Y. Xin, Z. Zhang, Y. Huang, Synthesis of functionalized 3D hierarchical porous carbon for high-performance supercapacitors, *Energy Environ. Sci.* 6 (2013) 2497.
- [20] J. Zhao, Z. Li, X. Yuan, Z. Yang, M. Zhang, A. Meng, Q. Li, A high-energy density asymmetric supercapacitor based on Fe<sub>2</sub>O<sub>3</sub> nanoneedle arrays and NiCo<sub>2</sub>O<sub>4</sub>/Ni(OH)<sub>2</sub> hybrid nanosheet arrays grown on SiC nanowire networks as free-standing advanced electrodes, *Adv. Energy Mater.* 8 (2018) 1702787.
- [21] M. Chhowalla, H.S. Shin, G. Eda, L.J. Li, K.P. Loh, H. Zhang, The chemistry of two-dimensional layered transition metal dichalcogenide nanosheets, *Nat. Chem.* 5 (2013) 263–275.
- [22] B. Anasori, M.R. Lukatskaya, Y. Gogotsi, 2D metal carbides and nitrides (MXenes) for energy storage, *Nat. Rev. Mater.* 2 (2017) 16098.
- [23] Q. Li, C. Lu, C. Chen, L. Xie, Y. Liu, Y. Li, Q. Kong, H. Wang, Layered NiCo<sub>2</sub>O<sub>4</sub>/reduced graphene oxide composite as an advanced electrode for supercapacitor, *Energy Storage Mater.* 8 (2017) 59–67.
- [24] Z.H. Huang, Y. Song, D.Y. Feng, Z. Sun, X. Sun, X.X. Liu, High mass loading MnO<sub>2</sub> with hierarchical nanostructures for supercapacitors, *ACS Nano* 12 (2018) 3557–3567.
- [25] K.L. Van Aken, M. Beidaghi, Y. Gogotsi, Formulation of ionic-liquid electrolyte to expand the voltage window of supercapacitors, *Angew. Chem. Int. Ed. Engl.* 54 (2015) 4806–4809.

- [26] W. Xing, S. Qiao, X. Wu, X. Gao, J. Zhou, S. Zhuo, S.B. Hartono, D. Hulicova-Jurcakova, Exaggerated capacitance using electrochemically active nickel foam as current collector in electrochemical measurement, *J. Power Sources* 196 (2011) 4123–4127.
- [27] R. Song, X. Li, F. Gu, L. Fei, Q. Ma, Y. Chai, An ultra-long and low junction-resistance Ag transparent electrode by electrospun nanofibers, *RSC Adv.* 6 (2016) 91641–91648.
- [28] C. Yuan, X. Zhang, L. Su, B. Gao, L. Shen, Facile synthesis and self-assembly of hierarchical porous NiO nano/micro spherical superstructures for high performance supercapacitors, *J. Mater. Chem.* 19 (2009) 5772.
- [29] V. Senthilkumar, F.B. Kadumudi, N.T. Ho, J.-W. Kim, S. Park, J.-S. Bae, W.M. Choi, S. Cho, Y.S. Kim, NiO nanoarrays of a few atoms thickness on 3D nickel network for enhanced pseudocapacitive electrode applications, *J. Power Sources* 303 (2016) 363–371.
- [30] Y. Wang, W. Lai, N. Wang, Z. Jiang, X. Wang, P. Zou, Z. Lin, H.J. Fan, F. Kang, C.-P. Wong, C. Yang, A reduced graphene oxide/mixed-valence manganese oxide composite electrode for tailorable and surface mountable supercapacitors with high capacitance and super-long life, *Energy Environ. Sci.* 10 (2017) 941–949.
- [31] Y. Zeng, Y. Han, Y. Zhao, Y. Zeng, M. Yu, Y. Liu, H. Tang, Y. Tong, X. Lu, Advanced Ti-doped Fe<sub>2</sub>O<sub>3</sub>@PEDOT core/shell anode for high-energy asymmetric supercapacitors, *Adv. Energy Mater.* 5 (2015) 1402176.
- [32] G. Li, X. Xu, R. Han, J. Ma, Synthesis and superior electrochemical properties of shaggy hollow Zn-doped Fe<sub>2</sub>O<sub>3</sub> nanospheres for high-performance lithium-ion batteries, *CrystEngComm* 18 (2016) 2949–2955.
- [33] F. Luan, G. Wang, Y. Ling, X. Lu, H. Wang, Y. Tong, X.X. Liu, Y. Li, High energy density asymmetric supercapacitors with a nickel oxide nanoflake cathode and a 3D reduced graphene oxide anode, *Nanoscale* 5 (2013) 7984–7990.
- [34] C. Guan, J. Liu, Y. Wang, L. Mao, Z. Fan, Z. Shen, H. Zhang, J. Wang, Iron oxide-decorated carbon for supercapacitor anodes with ultrahigh energy density and outstanding cycling stability, *ACS Nano* 9 (2015) 5198–5207.
- [35] R. Li, Y. Wang, C. Zhou, C. Wang, X. Ba, Y. Li, X. Huang, J. Liu, Carbon-stabilized high-capacity ferroferric oxide nanorod array for flexible solid-state alkaline battery-supercapacitor hybrid device with high environmental suitability, *Adv. Funct. Mater.* 25 (2015) 5384–5394.
- [36] M.F. El-Kady, R.B. Kaner, Scalable fabrication of high-power graphene micro-supercapacitors for flexible and on-chip energy storage, *Nat. Commun.* 4 (2013) 1475.
- [37] J. Zheng, Y. Zhang, Q. Wang, H. Jiang, Y. Liu, T. Lv, C. Meng, Hydrothermal encapsulation of VO<sub>2</sub>(A) nanorods in amorphous carbon by carbonization of glucose for energy storage devices, *Dalton Trans.* 47 (2018) 452–464.
- [38] J. Zhu, A.S. Childress, M. Karakaya, S. Dandeliya, A. Srivastava, Y. Lin, A.M. Rao, R. Podila, Defect-engineered graphene for high-energy- and high-power-density supercapacitor devices, *Adv. Mater.* 28 (2016) 7185–7192.
- [39] S. Dong, L. Shen, H. Li, G. Pang, H. Dou, X. Zhang, Flexible sodium-ion pseudocapacitors based on 3D Na<sub>2</sub>Ti<sub>3</sub>O<sub>7</sub> nanosheet arrays/carbon textiles anodes, *Adv. Funct. Mater.* 26 (2016) 3703–3710.
- [40] L. Zhang, P. Zhu, F. Zhou, W. Zeng, H. Su, G. Li, J. Gao, R. Sun, C.P. Wong, Flexible asymmetrical solid-state supercapacitors based on laboratory filter paper, *ACS Nano* 10 (2016) 1273–1282.